



OPEN ACCESS

EDITED BY

Yilin Fan,
UMR6607 Laboratoire de Thermique et Énergie
de Nantes (LTeN), France

REVIEWED BY

Dominique Tarlet,
Université de Nantes, France
Limin Wang,
Chinese Academy of Sciences (CAS), China

*CORRESPONDENCE

Tengzhou Xie,
✉ xtz@mail.hfut.edu.cn

RECEIVED 23 December 2023

ACCEPTED 07 March 2024

PUBLISHED 04 April 2024

CITATION

Yan H, Xie T, Li J, Fan J and Dai X (2024), Drag
reduction of Clark-Y hydrofoil by biomimetic
fish scale structure under the condition of
biomimetic jet.
Front. Energy Res. 12:1360495.
doi: 10.3389/fenrg.2024.1360495

COPYRIGHT

© 2024 Yan, Xie, Li, Fan and Dai. This is an open-
access article distributed under the terms of the
[Creative Commons Attribution License \(CC BY\)](https://creativecommons.org/licenses/by/4.0/).
The use, distribution or reproduction in other
forums is permitted, provided the original
author(s) and the copyright owner(s) are
credited and that the original publication in this
journal is cited, in accordance with accepted
academic practice. No use, distribution or
reproduction is permitted which does not
comply with these terms.

Drag reduction of Clark-Y hydrofoil by biomimetic fish scale structure under the condition of biomimetic jet

Hao Yan¹, Tengzhou Xie^{1*}, Jian Li¹, Jinchuan Fan² and Xinyue Dai²

¹School of Mechanical Engineering, Hefei University of Technology, Hefei, China, ²Intelligent Manufacturing Institute of HFUT, Hefei, China

Hydrofoil, as the basic shape of the fluid blade, is widely used in fluid transport and energy conversion. However, friction resistance and pressure differential resistance are generated in the hydrofoil flow process, resulting in substantial energy consumption and negatively affecting the economy. On this basis, we propose two drag-reducing structures based on Clark-Y hydrofoil. In the design process of the jet structure, we considered the bionic jet velocity, jet angle and jet structure position as the design parameters and obtained the optimal jet structure by using Taguchi method. Finally, the two schemes (Clark- Y_{ori} and Clark- Y_{opt}) are numerically simulated using large eddy simulation. Results show that when $U_{jet} = 1.44$ m/s, $\theta = 3^\circ$ and $x = 18.6$ mm, the jet structure can play a significant drag reduction effect. Compared with Clark- Y_{ori} , the drag coefficient of Clark- Y_{opt} is reduced by 26.5%, and the lift drag ratio is increased by 16.4%. Compared with Clark- Y_{ori} , Clark- Y_{opt} can reduce the wall shear stress of the leading edge of the hydrofoil, thereby diminishing the frictional resistance. Meanwhile, the jet structure can effectively balance the area of the low-pressure region on the suction side of the hydrofoil, significantly reducing the pressure differential resistance. Clark- Y_{opt} can accelerate the vortex collapse that decreases turbulence intensity and turbulence resistance. Moreover, it can effectively block the near-wall reflux of hydrofoil and reduce the internal friction between the reflux and the main flow.

KEYWORDS

biomimetic fish scale drag reduction, biomimetic jet drag reduction, large eddy simulation, Taguchi algorithm, hydrofoil

1 Introduction

Hydrofoil, as the basic shape of the fluid blade, plays an important role in the fluid transport and energy conversion and is mostly used in shipping and navigation vehicles and other fields (Lv et al., 2013; Shen et al., 2022; Liu et al., 2023). When the ship or vehicle moves forward, the fluid passing around the hydrofoil produces resistance, such as friction resistance and pressure differential resistance, which is extremely unstable. As a result, energy consumption increases and the navigation economy declines. An in-depth investigation shows that because of the instability of the flow, where the flow transitions from layer to turbulent flow, the velocity gradient between the fluids increases, exhibiting frictional resistance, differential pressure resistance and other

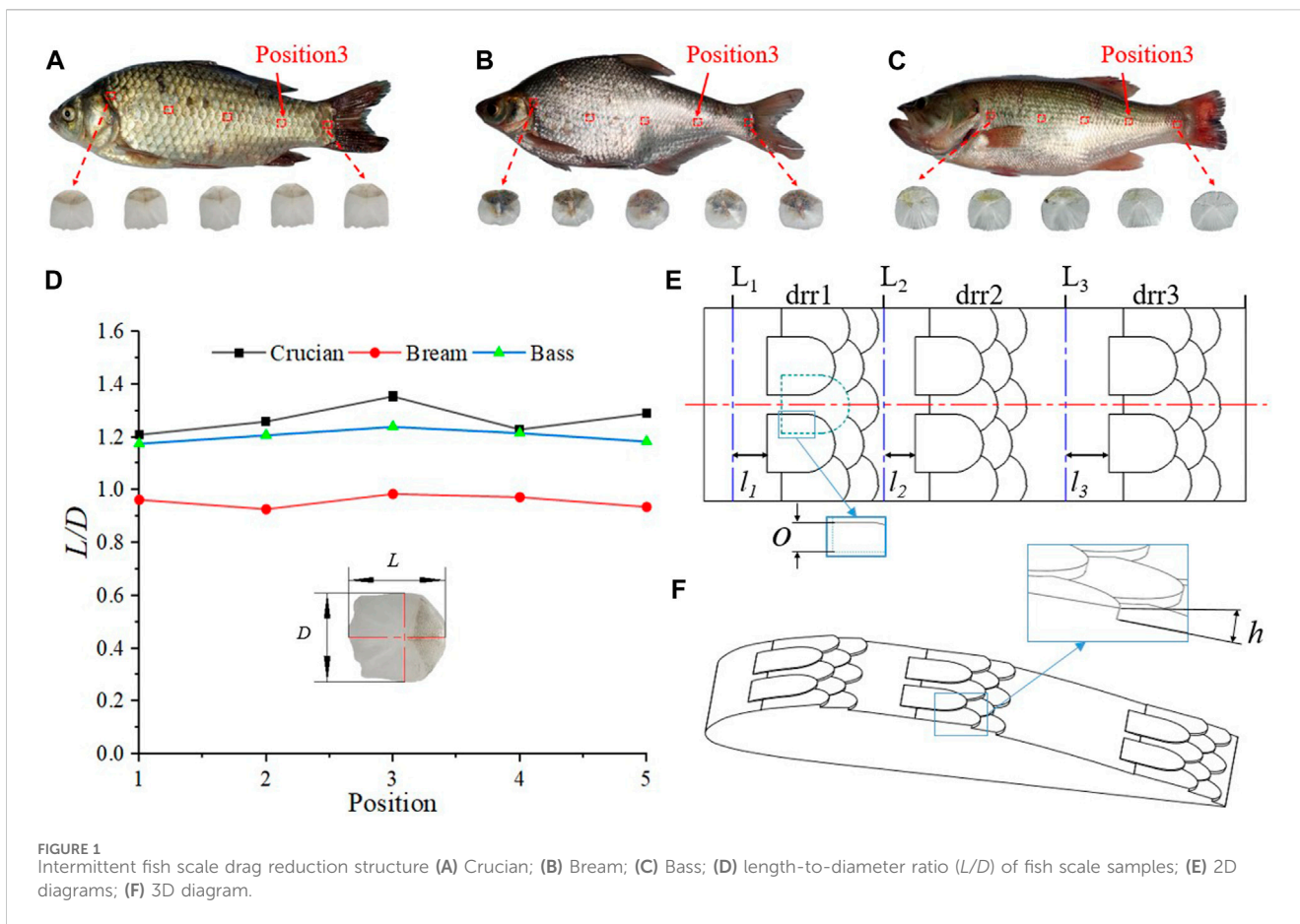
resistance. The wall surface with hydrophobic characteristics causes the turbulent boundary layer to slip and reduce Reynolds stress, thereby diminishing turbulence and reducing drag (Nowrouz Mohammad et al., 2012; Nowrouz Mohammad et al., 2013). Injecting air into the turbulent boundary layer to form an air layer also affects the near-wall turbulent structure and inhibits Reynolds stress, achieving a better drag reduction effect (Park et al., 2015; Feng Yan-Yan et al., 2020; Zhang et al., 2021). The effective suppression of various drags caused by turbulence has important research significance in solving engineering application problems. Therefore, the research on optimising drag reduction performance is urgent.

Bionics, as a subject of studying the law of biological evolution to obtain technical methods to solve practical engineering problems, has been the focus of researchers in recent years, and some achievements have been made in the exploration process. Fish has evolved on the earth for hundreds of millions of years and is the most widely distributed aquatic organism. The fish scale structure, as the most common component structure, has shown excellent drag reduction performance and is a natural non-smooth drag reduction structure (Dou et al., 2012; Muthuramalingam et al., 2019; Muthuramalingam et al., 2020; Wang et al., 2021; Ganesh Natarajan and Bruce Ralphin Rose, 2022). Therefore, the fish scale structure has unique research potential in the field of bionic drag reduction. Muthukumar et al. (Muthuramalingam et al., 2019; Muthuramalingam et al., 2020) conducted a geometric reconstruction of the topological structure of the European perch scale surface on a plate and performed numerical and experimental flow simulations. They found staggered velocity stripes with a velocity difference of approximately 9% on the fish scale array surface, indicating that the existence of the fish scale array resulted in stable low and high-speed stripes. These regularly arranged fringe structures can inhibit the transition of layers to turbulent flow. In a follow-up study, they found that the fish scale array has a delay effect of approximately 55% on the TS wave, further proving its drag reduction performance. They pointed out that the theoretical drag reduction effect can reach 27%. Ganesh Natarajan S et al. (Ganesh Natarajan and Bruce Ralphin Rose, 2022) examined the drag reduction effect at various angles of attack at a specific Reynolds number by using 3D-printed bionic fish scale film pasted on NACA0021. They achieved the maximum drag reduction rate of 9.57% at 0° angle of attack and pointed out that the angle of attack for the best drag reduction performance is between 0° and 10°. Their analysis revealed that the fish scale structure reduces the shear stress of the aerofoil wall, resulting in drag reduction. Dou et al., 2012 analysed the surface microstructure of fish scales and found micron-scale caves on the surface. The results showed that under low-pressure conditions, due to flow separation and eddy current, the gas phase was generated at the solid-liquid surface, and part of the solid-liquid shear force was replaced by gas-liquid shear force, thereby reducing the friction resistance. Wang et al., 2021 studied the microscopic morphology of *Sciaenops ocellatus* and the arrangement of fish scales and then prepared biomimetic fish scale surfaces with hydrophobic properties using laser processing. Compared with an aluminium alloy surface, the drag reduction rate of biomimetic fish scale surface under

laminar flow conditions can reach 4.814%. They pointed out that drag reduction performance decreases gradually as the transition from layer to turbulent flow occurs.

In addition to the exploration of the bionic fish scale drag reduction structure, the researchers proposed another drag reduction idea, namely, jet drag reduction. Yunqing Gu et al. (Gu et al., 2014) proposed a biomimetic jet surface based on shark gills. A frictional torque test was carried out on the smooth surface and biomimetic jet surface through a torque signal coupler at different rotational speeds, and the results showed that the biomimetic jet surface could thicken the viscous bottom and reduce the shear stress on the wall, as well as the frictional resistance. When Li et al., 2017 studied the jet surface model of the bionic shark's gills, they found that a smaller jet angle is preferred when the velocity ratio remains unchanged. When the jet angle is fixed, a greater flow rate ratio indicates better drag reduction effect. In addition, they proposed that the bionic jet changes the flow structure of the turbulent boundary layer, increases the thickness of the viscous bottom layer and reduces the normal velocity gradient of the wall, thereby decreasing the friction resistance. Chen et al., 2021 studied the influence mechanism of jet on flow resistance through the structure of shark gill jet. The results showed that jets can reduce the boundary layer on the surface of objects, producing a drag-reduction effect. The drag reduction effect is improved with the increase in jet velocity, and the curved nozzle is more conducive to reducing drag. Bedri et al. (Yagiz et al., 2012) used a flow control device to study the feasibility of a 2D profile bump and an independent jet actuator. They also explored a hybrid control that integrates the two elements to mitigate the shock wave and thus minimize wave resistance during transonic flight conditions. The results showed that after optimising the relevant design parameters, the total resistance was reduced by 3.94% and the lift was increased by 5.03%. Shen et al., 2018 studied drag reduction efficiency and heat flow reduction efficiency of unit mass reverse jet. The results showed that under the pre-treatment requirements of reducing drag and heat flow, the reduction efficiency of drag and heat flow can be improved by optimising jet temperature and pressure, which is conducive to saving occupied space, reducing system weight and promoting vehicle loading. Kim et al., 2020 studied the drag reduction parameters of countercurrent jet in supersonic flow through numerical simulation. The results showed that amongst the five relevant parameters, jet mass flow is the dominant factor in drag reduction and transition of countercurrent jet, and the nozzle size has little influence on drag reduction. In addition, under high-temperature conditions, an appropriate trade-off between each parameter is crucial to obtain the maximum drag reduction rate. The methods of biomimetic fish scale and jet drag reduction are both effective in drag reduction. Organically combining these approaches can achieve a more effective hybrid drag reduction structure.

Taguchi method, as an orthogonal experimental design algorithm, can obtain the optimal parameter combination with the least number of experiments and the lowest cost under the action of multiple parameters. Li et al. (Yan et al., 2022) obtained the optimal active jet structure through the Taguchi design of three parameters, namely, jet position, jet ratio and angle between jet and aerofoil surface, reducing the cavitation volume of the aerofoil to only 29.95% of the original aerofoil. Wang et al. (Wang et al., 2021a;



Wang et al., 2021b) carried out the Taguchi design of the fluidised bed gas chamber and the airway and conducted numerical and experimental analyses to obtain the parameter combination with the lowest powder discharge residual rate and the best velocity distribution uniformity. Bai et al., 2022 carried out Taguchi design on eight parameters of the impeller meridian profile of the submersible electric pump, resulting in a 3.5% increase in head and a 6.1% increase in efficiency after model optimisation. Feng et al. (Feng Guozeng et al., 2020) used the Taguchi method to analyse the influence of three channel parameters of the air distributor on the drag coefficient, and the difference between the predicted results and the simulated results was 4.9%, providing a performance reference for the local manufacturing and early development of the air distributor. Kotcioglu et al., 2013 designed Taguchi experiments on six design parameters of the heat exchanger, including the ratio of duct width to height, the ratio of winglet length to duct length, winglet angle, Reynolds number, flow rate and pressure drop. They also optimised the heat exchanger to obtain the minimum pressure drop and maximum heat transfer.

In summary, bionic fish scale drag reduction and jet drag reduction are effective methods. If the two can be organically combined, then an improved hybrid drag reduction structure can be obtained. On this basis, Clark-Y hydrofoil is considered the research object, and different types of drag reduction structures are proposed: intermittent bionic fish scale structure, bionic fish gill jet structure and bionic fish scale hybrid drag reduction structure. The former is considered the basic structure, and we

replaced the fish scale drag reduction structure of the front edge of the hydrofoil with a jet structure. Then, we obtained the optimal combination of jet parameters through the Taguchi method to achieve the optimal hybrid drag reduction structure. Finally, a large eddy simulation was used to analyse the influence of the two drag reduction structures on the drag reduction of the hydrofoil. This study aims to provide a reference for further research on drag reduction.

2 Model building and numerical calculation

2.1 Design of fish scale drag reduction structure

The current research literature indicates that fish scale structure has great potential for fluid drag reduction. As shown in Figure 1, the fish scale samples were obtained from crucian carp, Bream, and perch obtained from the market. These three types of freshwater fish are widely distributed and easily obtained, and their scale sizes and distribution densities are relatively different. Such differences are necessary for the study of the macroscopic size of fish scales. In the process of fish scale sampling, the lateral scale of each fish was considered the central sampling line (Position3), and two sampling lines were obtained equidistant from the upper and lower sides. On each sampling line, five fish scales were obtained equidistant from

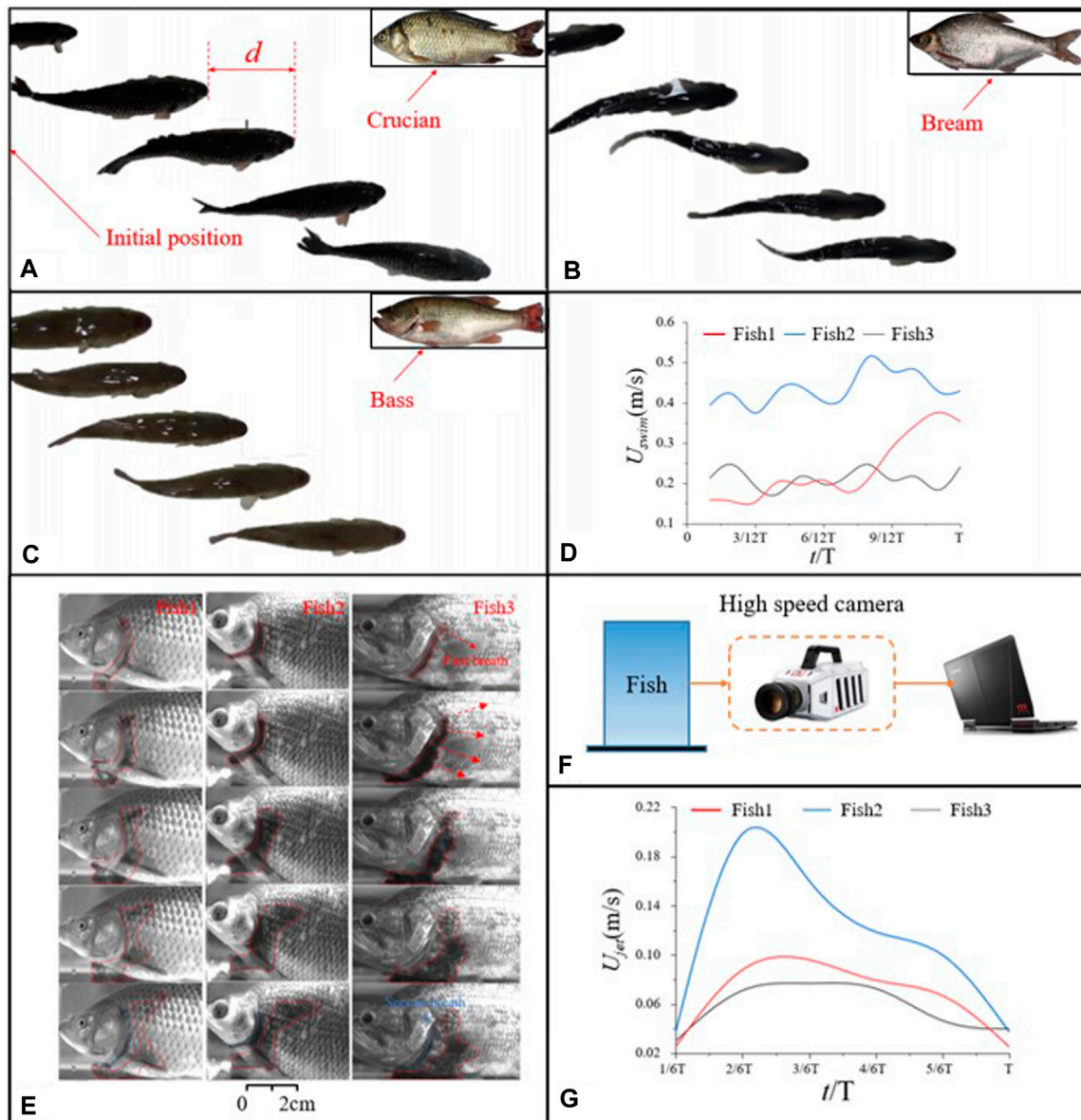
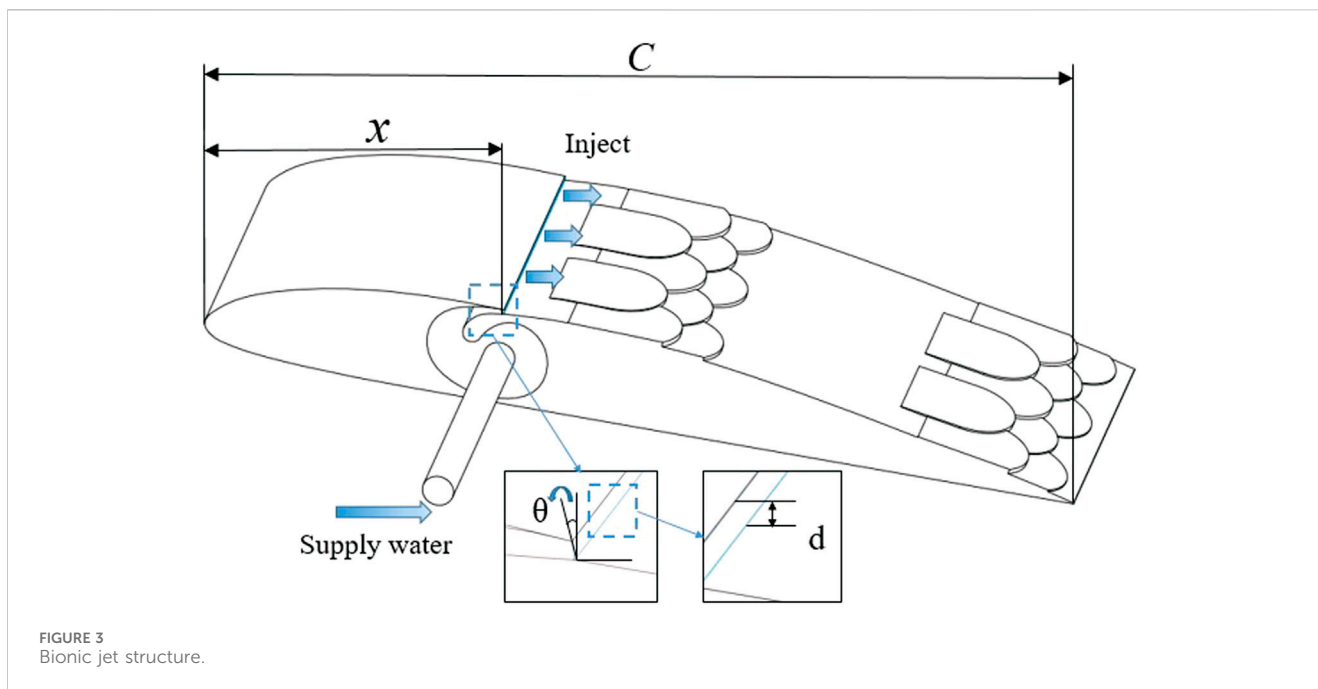


FIGURE 2 Fish swimming in a cycle: (A) Crucian; (B) Bream; (C) Bass; (D) Swimming speed of the three fish; (E) Breathing cycles of the three fish species; (F) Schematic obtained using high-speed photography cameras; (G) acquired gill jet velocity; To obtain the jet parameters formed by the gills breathing, we initially measured the swimming under normal conditions, determined the range that could be photographed by the camera as a period and measured the speed of the fish in a period based on the position of the fish head. (A), (B) and (C) show the swimming process of the three fish types in a cycle. To obtain more accurate data, we have carried out multiple measurements for each fish type, using the average value of the measured results as the data to draw the swimming speed changes of fish in a cycle, as shown in (D).

the gills to the tail, and the surface of the sample was cleaned with ethanol solution. To standardize the sample size, a dimensionless approach is adopted, wherein the aspect ratio (L/D) is used as the size reference (Ganesh Natarajan and Bruce Ralphin Rose, 2022). In this study, the length–diameter ratio of samples on each sampling line was averaged, as shown in Figure 1D. After averaging, the length–diameter ratio of the samples on each sampling line was statistically sorted out, and the average length–diameter ratio obtained from all sampling lines was averaged again, until the average length–diameter ratio of all samples was finally obtained, that is, $L/D = 1.165$. Therefore, the diameter of the circular section of

the fish scale was set to $D = 6.00$ mm in this study, and the length is $L = 6.99$ mm. As shown in Figure 1E, the suction side of the hydrofoil (with a string length of 56 mm) is divided into three drag reduction regions (drr1, drr2, drr3), in which drr1 is between the dividing line L_1 and L_2 , drr2 is between L_2 and L_3 , and drr3 is between L_3 and the tail edge of the hydrofoil. Moreover, the dividing line L_1 is 3 mm from the leading edge of the hydrofoil. L_2 is 18.60 mm from the front of the hydrofoil, and L_3 is 37.20 mm from the front of the hydrofoil. The distance between the fish scale structure (total length 11.50 mm) in each drag reduction area and the dividing line was l_1, l_2 , and l_3 , respectively, where $l_1 = 0.96$ mm,



$l_2 = 1.51$ mm and $l_3 = 6.66$ mm. The overlapping size of the adjacent fish scales $O = 2$ mm, and the thickness of each fish scale $h = 0.36$ mm.

2.2 Acquisition of bionic jet parameters

We obtain the relevant parameters of the gill jet by using pigments that are more distinguished from water and observing the process of their outward diffusion through the gills with a high-speed camera. The fish have a relatively short respiratory cycle; thus, we set the fps of the high-speed camera to 300 frames to obtain a complete gill jet cycle, as shown in Figure 2F of the high-speed camera placement. Figure 2E shows the entire cycle of gill respiration and pigment diffusion. We measured the pigment diffusion speed with one gill breath as a cycle and obtained the gill jet velocity of three types of fish through multiple measurements and averaging, as shown in Figure 2G. As shown in Figure 2E, the main body of pigment exhaled through the gills diffuses backward, but some pigments diffuse to the bottom of the gills. The pigment that diffuses to the bottom of the gills accumulates at the bottom because of the limited volume of the container, obtaining inaccurate result. Figure 2G shows that the pigment speed exhaled through fish gills increases continuously at the initial stage, reaching a peak value at approximately $5/12T$, and then the pigment continues to diffuse whilst the speed decreases continuously. The initial diffusion speed of pigment continues to increase because the exhalation stage of fish lasts for a while.

To obtain the bionic jet parameters, we define the jet scale: $S_{jet} = U_{jet}/U_{swim}$, where U_{swim} takes the average value of the whole period. U_{jet} takes the average value of the intermediate time region because of the large error between the initial and the end of the gill jet, and the S_{jet} of the three fish is finally calculated as 0.30, 0.32, and 0.29; thus, $0.29 \leq S_{jet} \leq 0.32$.

2.3 Experimental design of Taguchi algorithm

In our previous research, the bionic jet structure played a significant role in inhibiting cavitation. We also analysed its lift resistance characteristics, and found that it has excellent effects in reducing drag (Yan et al., 2022). In the study of fish scale drag reduction, we found that at low speeds, the drag reduction effect of fish scale during the flow around hydrofoil is considerable. This condition is caused by the fish scale structure that can effectively inhibit the reflux near the wall of the hydrofoil and transform the fluid flow state into laminar flow, greatly reducing the turbulent resistance. However, with the increase in flow velocity, the fluid cannot easily maintain a laminar flow state. Thus, transition to a turbulent state is achieved. On this basis, we change the drr1 drag-reducing structure of the new intermittent fish-scale structure into a bionic jet structure, so that the two can be organically combined to obtain a hydrofoil with excellent drag-reducing performance at high speed.

As shown in Figure 3, in the bionic jet structure, jet velocity, jet angle and starting position are important dimension parameters. In Section 2.2, we measured that the ratio of the bionic jet is $0.29 \leq S_{jet} \leq 0.32$, whereas the mainstream velocity is $U_{\infty} = 4.5$ m/s. Therefore, the swimming velocity of fish is similar to the mainstream velocity of hydrofoil. The jet velocity of fish gills is similar to that of biomimetic jets, so the range of biomimetic jet velocity obtained after similarity transformation is 1.305 m/s $\leq U_{jet} \leq 1.440$ m/s. Our previous research on drag reduction of fish scale structure indicated that the distance between the farthest return of hydrofoil near the wall and the leading edge of hydrofoil was 16.8 mm $\leq x \leq 18.6$ mm (where the chord length of hydrofoil $C = 56$ mm), and the backflow was mostly concentrated in the range of 9° outside the suction side based on the tangent line of hydrofoil near the wall. Therefore, our jet slot was considered the normal line. The angle of

TABLE 1 Factors and levels selected to be analysed.

Factor	Symbol	Level of factors			
		Level-1	Level-2	Level-3	Level-4
Jet velocity	U_{jet}	1.305	1.350	1.395	1.440
Jet angle	θ	0°	3°	6°	9°
Starting position	x	16.8	17.4	18.0	18.6

TABLE 2 Standard L_{16} OA with factors and level.

Trial no	Factors and their level		
	U_{jet}	θ	x
1	1	1	1
2	1	2	2
3	1	3	3
4	1	4	4
5	2	1	2
6	2	2	1
7	2	3	4
8	2	4	3
9	3	1	3
10	3	2	4
11	3	3	1
12	3	4	2
13	4	1	4
14	4	2	3
15	4	3	2
16	4	4	1

counterclockwise rotation is considered the jet angle. Thus, $0^\circ \leq \theta \leq 9^\circ$, where the jet slit width $d = 0.005 C = 0.28 \text{ mm}$ (Yan et al., 2022). Therefore, to seek the best jet structure arrangement scheme, based on the above studies, the jet velocity U_{jet} , jet angle θ and starting position x are considered the control factors, and the hydrofoil lift drag ratio k and drag coefficient C_d are considered the response factors. Moreover, different contribution degrees of each control factor to the response factors are obtained by Taguchi method. On this basis, the optimal design parameter combination is selected. In this study, four-level values with equal spacing are selected for the three control factors within an appropriate range. The selected control factors and their specific level values are shown in Table 1. By analysing the influence of these control factors on the response factors after the combination of different level values, the different contribution degrees of each control factor to the response factors can be obtained, and the optimal parameter combination can be selected.

The traditional three-factor and four-level experiments require 64 trials to enable the different factors to fully influence the results.

This condition is evidently a tremendous test workload. Therefore, the Taguchi method provides an orthogonal array table, and only 16 tests are required to obtain the influence of each factor for three factors and four levels, greatly improving the test efficiency, as shown in Table 2.

2.4 Numerical calculation

2.4.1 Boundary conditions and governing equations

ANSYS Fluent software based on the finite volume method is often used for simulation analysis. The calculation area is shown in Figure 4. The total length of the fluid domain is 14°C , the width is 3.4°C , and the spanwise span is 0.36°C . The total length of the body of influence (boi) region is 1.75°C , the width is 0.5°C , and the distance velocity inlet of the hydrofoil front is 5 C. In this study, the attack angle of the aerofoil is 8° , the inlet velocity is 4.5 m/s, and the outlet is set as the pressure outlet, corresponding to the cavitation number of 0.8. The SIMPLE algorithm is used to solve the coupling of the velocity field and pressure field. The diffusion term is interpolated by the least square method, the convection term is discretised by a bounded central difference scheme, and the turbulent transport equation and some scalar equations are discretised by second-order upwind.

2.4.2 Numerical method

In the study, we used LES to assay the surrounding fluid state of the hydrofoil. In LES, large-scale turbulence was directly solved using a low-pass filter, and small-scale turbulence was processed by subgrid-scale (SGS) (Yan et al., 2022). The relevant continuity and momentum equations are as follows:

$$\frac{\partial \rho_c}{\partial t} + \frac{\partial (\rho_c u_i)}{\partial x_i} = 0 \tag{1}$$

$$\frac{\partial (\rho_c u_j)}{\partial t} + \frac{\partial (\rho_c u_i u_j)}{\partial x_j} = \frac{\partial}{\partial x_i} \left(\mu_c \frac{\partial u_i}{\partial x_j} \right) - \frac{\partial p}{\partial x_i} \tag{2}$$

where p is the pressure of the compound, u_i is the velocity component, and μ_c and ρ_c represent the viscosity and density of the compound, respectively. LES is a simulation technique that resolves the large-scale turbulent structures whilst modelling the smaller scales. Eqs 1, 2 are usually separated into two sections: subgrid-scale (SGS) and grid-scale (GS), which are computed using Favre filtering. The calculation results are shown in equation 3, 4:

$$\frac{\partial \rho_c}{\partial t} + \frac{\partial (\rho_c \bar{u}_j)}{\partial x_j} = 0 \tag{3}$$

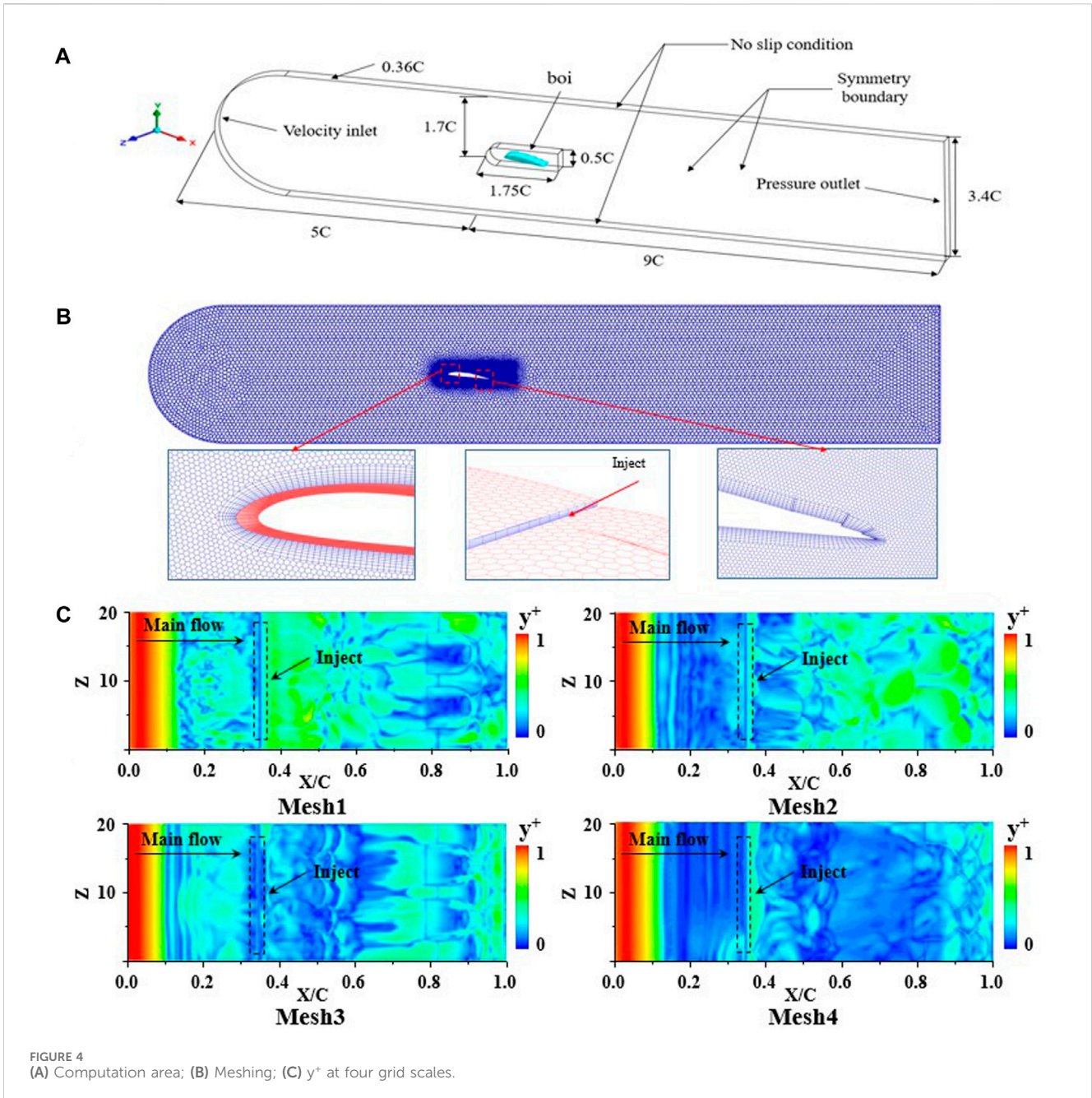


FIGURE 4 (A) Computation area; (B) Meshing; (C) y^+ at four grid scales.

$$\frac{\partial(\rho_c \bar{u}_j)}{\partial t} + \frac{\partial(\rho_c \bar{u}_i \bar{u}_j)}{\partial x_j} = \frac{\partial}{\partial x_j} \left(\mu_c \frac{\partial \bar{u}_i}{\partial x_j} \right) - \frac{\partial \bar{p}}{\partial x_i} - \frac{\partial \tau_{ij}}{\partial x_j} \quad (4)$$

$$\bar{S}_{ij} = \frac{1}{2} \left(\frac{\partial \bar{u}_i}{\partial x_j} + \frac{\partial \bar{u}_j}{\partial x_i} \right) \quad (7)$$

The stress tensor τ_{ij} of SGS is expressed as follows:

$$\tau_{ij} = \rho_c (\overline{u_i u_j} - \bar{u}_i \bar{u}_j) \quad (5)$$

τ_{ij} in Eq. 5 needs to be modelled. Eddy current or subgrid viscosity μ_s is commonly used in subgrid modelling and can be computed using various technical methods. In the eddy viscosity model, these variables are represented in Equation 6, 7:

$$\tau_{ij} = \frac{2}{3} - 2\mu_s \bar{S}_{ij} \quad (6)$$

2.4.3 Grid division and grid independence verification

When the fluid domain involves relatively complex structures, unstructured meshing can also satisfy the simulation requirements. Therefore, in this study, we used Fluent meshing, and we sequentially encrypted the boi region and ensured that y^+ was less than 1 to verify grid independence. Under the premise that the maximum size of the global mesh is 5 mm, the local maximum mesh size of the boi region is set to 0.30, 0.25, 0.20, and 0.15 mm, and

TABLE 3 Comparison of C_l and C_d of four grid types.

Mesh	Nodes	C_l	C_d
Mesh1	647876	0.868	0.126
Mesh2	948689	0.875	0.128
Mesh3	1428676	0.876	0.127
Mesh4	2441788	0.877	0.126

TABLE 4 Lift coefficients and drag coefficients of Clark-Y.

	C_l	C_d
Wang ^{exp}	0.76	0.119
Yan	0.78	0.13
Li	0.781	0.132
The result of this paper	0.766	0.122

the mesh is gradually encrypted in turn. At the same time, the boundary layer mesh is set as follows: the height of the first layer mesh is set to 0.10 mm, the number of layers is set to 8, and the generation method is uniform.

In this study, one of the drag reduction schemes ($U_{jet} = 1.44 \text{ m/s}$, $\theta = 3^\circ$, $x = 18.6 \text{ mm}$) is considered, and the average lift coefficient C_l and average drag coefficient C_d are used as the evaluation criteria to verify the grid independence. The relevant definitions are as follows: $C_l = F_l / (0.5 \rho U_\infty^2 A)$, $C_d = F_d / (0.5 \rho U_\infty^2 A)$, where F_l and F_d represent the lift and drag force of the aerofoil, respectively; ρ is the density of the medium, U_∞ is the velocity of the aerofoil at infinity, and A is generally the chord length of the aerofoil multiplied by the span.

As shown in Table 3, the comparison of C_l and C_d of the underwater wing of the four mesh scales shows that the coefficient values change with the increase in the number of grids, but the amplitude of change is different from the former. The change rates of C_l between adjacent grids are 0.8%, 0.1% and 0.1%, and the change rates of C_d are 1.58%, 0.7%, and 0.7%. At the same time, as shown in Figure 4C, y^+ decreases with the increase in the number of grids, and y^+ can be less than 1 under the four grid scales. By comprehensive comparison, the fluctuation amplitude of C_l , C_d and y^+ of the Mesh4 scheme are relatively smaller. Thus, the influence of mesh4 mesh scale on the calculation results can be ignored, and it can accurately predict the flow state of fluid and the lift resistance characteristics of hydrofoil.

2.4.4 Verification of numerical methods

The chord length and span of the aerofoil used in this study are different from the data in the public literature. Thus, the dimension parameters used in the numerical method verification are the same as those in the references, that is, the chord length of the aerofoil is 70 mm and the span is 21 mm. The proposed numerical method verifies that the Clark-Y hydrofoil is selected for numerical simulation under the condition of an 8° angle of attack and 10 m/s mainstream velocity. On the basis of the Reynolds number of chord length at 7×10^5 , cavitation number at 0.8 and cavitation model at Sauer model, we

TABLE 5 Results of the response variable.

Test run	U_{jet}	θ	x	k	C_d
L01	1.305	0°	16.8	5.8207	0.1625
L02	1.305	3°	17.4	5.7556	0.1640
L03	1.305	6°	18.0	5.7594	0.1632
L04	1.305	9°	18.6	5.8266	0.1630
L05	1.350	0°	17.4	5.7600	0.1644
L06	1.350	3°	16.8	5.8359	0.1619
L07	1.350	6°	18.6	5.8381	0.1595
L08	1.350	9°	18.0	5.7890	0.1650
L09	1.395	0°	18.0	5.7907	0.1618
L10	1.395	3°	18.6	5.8590	0.1610
L11	1.395	6°	16.8	5.7901	0.1647
L12	1.395	9°	17.4	5.7910	0.1628
L13	1.440	0°	18.6	5.9037	0.1608
L14	1.440	3°	18.0	5.8413	0.1622
L15	1.440	6°	17.4	5.8055	0.1647
L16	1.440	9°	16.8	5.7510	0.1621

adopt the same boundary conditions as the references. The C_l obtained by simulation is compared with C_d . As shown in Table 4, the data are C_l and C_d after a similar transformation between the published literature and the numerical results in this study. Compared with the experimental results of Wang (Wang et al., 2001) and the numerical simulation results of Yan (Yan et al., 2020; Yan et al., 2021) and Li (Yan et al., 2022), the C_l errors are 0.7%, 1.7% and 1.9%, and the C_d errors are as follows: 0.8%, 6%, and 7.5%. The coefficient error of the numerical simulation results can be controlled to 8% when compared with the experimental results or the published data, verifying the accuracy of the proposed numerical method and the reliability of the grid division.

3 Result analysis of Taguchi algorithm

3.1 Analysis of signal-to-noise ratio

In Taguchi's algorithm, the signal-to-noise ratio (S/N) refers to the power ratio of signal to noise. It is generally divided into three signal-to-noise ratios, namely, large-the-better (LTB), small-the-better (STB) and nominal-the-better (NTB) (Wang et al., 2021a; Wang et al., 2021b), whose definition formulas are shown as Equation 8, 9, 10:

$$S/N = -10 \log \frac{1}{n} \left(\sum \frac{1}{y^2} \right) \tag{8}$$

$$S/N = -10 \log \frac{1}{n} (\sum y^2) \tag{9}$$

$$S/N = 10 \log \frac{\bar{y}^2}{s_y^2} \tag{10}$$

TABLE 6 Response table for signal-to-noise Ratios(k).

Level	Factors		
	U_{jet}	θ	x
1	15.25	15.30	15.27
2	15.28	15.30	15.24
3	15.28	15.27	15.26
4	15.31	15.25	15.35
Delta	0.05	0.05	0.12
Rank	2	3	1

TABLE 7 Response table for signal-to-noise ratios (C_d).

Level	Factors		
	U_{jet}	θ	x
1	15.75	15.79	15.77
2	15.77	15.80	15.70
3	15.78	15.76	15.75
4	15.79	15.74	15.86
Delta	0.04	0.05	0.16
Rank	3	2	1

For the two responses in this study, a higher lift–drag ratio is preferred. Thus, the signal-to-noise ratio with high hope characteristics is selected. A smaller drag coefficient achieves better performance, so the signal-to-noise ratio of the desired characteristic is selected. Through numerical simulation, the lift–drag ratio k and drag coefficient C_d of the aerofoil of each scheme are obtained, as shown in Table 5.

Based on the numerical calculation results of each scheme k and C_d in Table 5, the SNR response of each factor level is calculated, as shown in Tables 6, 7, where Delta is the difference between the maximum and minimum S/N ratio average response of each factor. A greater Delta value indicates greater contribution of the corresponding factor to the SNR response, and *vice versa*. As shown in Table 6, when the SNR response is k , factor x (Delta = 0.12, Rank = 1) contributes the most to the SNR response, and factor U_{jet} (Delta = 0.05, Rank = 2) and factor θ (Delta = 0.05, Rank = 3) contribute the least. When the SNR response is C_d , in Table 7, factor x (Delta = 0.16, Rank = 1) contributes the most to the SNR response, and factor θ (Delta = 0.05, Rank = 2) and factor U_{jet} (Delta = 0.04, Rank = 3) contribute the least.

3.2 Main effect diagram analysis

The analysis results indicate that each control factor has a different contribution degree to the response factor, that is, a major factor affects the response, referred to as the main effect. A larger slope of the curve indicates a more evident main effect. In

the main effect diagram of k , as shown in Figure 5A, factor x has the largest main effect value, followed by factor U_{jet} and θ . In the main effect diagram of C_d , as shown in Figure 5B, factor x has the largest main effect value, followed by factor θ , and factor U_{jet} has the smallest main effect value. The analysis of the main effect diagram of k and C_d indicates that the position of the jet structure greatly influences the variation of the lift–drag ratio and drag coefficient of the hydrofoil, and the drag reduction performance of the hydrofoil can be optimised when the maximum lift–drag ratio is obtained.

4 Result analysis

The above analysis illustrates that when $U_{jet} = 1.44$ m/s, $\theta = 3^\circ$, and $x = 18.6$ mm, the lift–drag ratio of hydrofoil is the largest and the drag coefficient is the smallest. To study and verify the lift resistance characteristics under the optimal combination of factors, we perform transient analysis on the original scheme (Clark-Y_{ori}) and the optimal scheme with jet structure (Clark-Y_{opt}), as follows:

4.1 Lift resistance characteristic analysis

As shown in Figure 6 and Table 8, in terms of the transient change of lift coefficient, Clark-Y_{opt} is lower than Clark-Y_{ori} most of the time because the low-pressure area on the suction side of Clark-Y_{opt} is reduced after the addition of jet structure, thereby weakening the hydrofoil lift, which is reflected in the average result. The lift coefficient of Clark-Y_{opt} decreased by 12.2%. The drag coefficient of Clark-Y_{opt} is lower than that of Clark-Y_{ori} during most of the transient changes, because the jet structure can block the return flow near the wall of the hydrofoil to reduce the friction resistance. In addition, the reduction of the low-pressure area minimises the pressure differential resistance, which is reflected in the average result. The drag coefficient of Clark-Y_{opt} decreased by 26.5%. The lift–drag ratio of Clark-Y_{opt} is superior to that of Clark-Y_{ori} most of the time. Thus, Clark-Y_{opt} obtains better hydraulic characteristics, reflecting the average result. The lift–drag ratio of Clark-Y_{opt} increases by 16.4%.

Although the lift of Clark-Y_{opt} is decreased, its drag is greatly reduced, and the lift–drag ratio is increased to a certain extent. These findings indicate that the addition of jet structure can reduce the drag and increase the lift–drag ratio, verifying the reliability of Taguchi's method.

4.2 Analysis of friction resistance and shear stress

As shown in Figure 7, the transient change in the friction-resistance coefficient, Clark-Y_{opt} is lower than Clark-Y_{ori} in most of the same period, but it also increases in part of the time, which is reflected in the average result. Its frictional resistance coefficient is reduced by only 5.4%.

As shown in Figure 8, to further analyse the frictional resistance, we studied the transient distribution of shear stress on the wall of the two hydrofoils. After comparative analysis, we obtained the following: Compared with Clark-Y_{ori}, the wall shear stress of

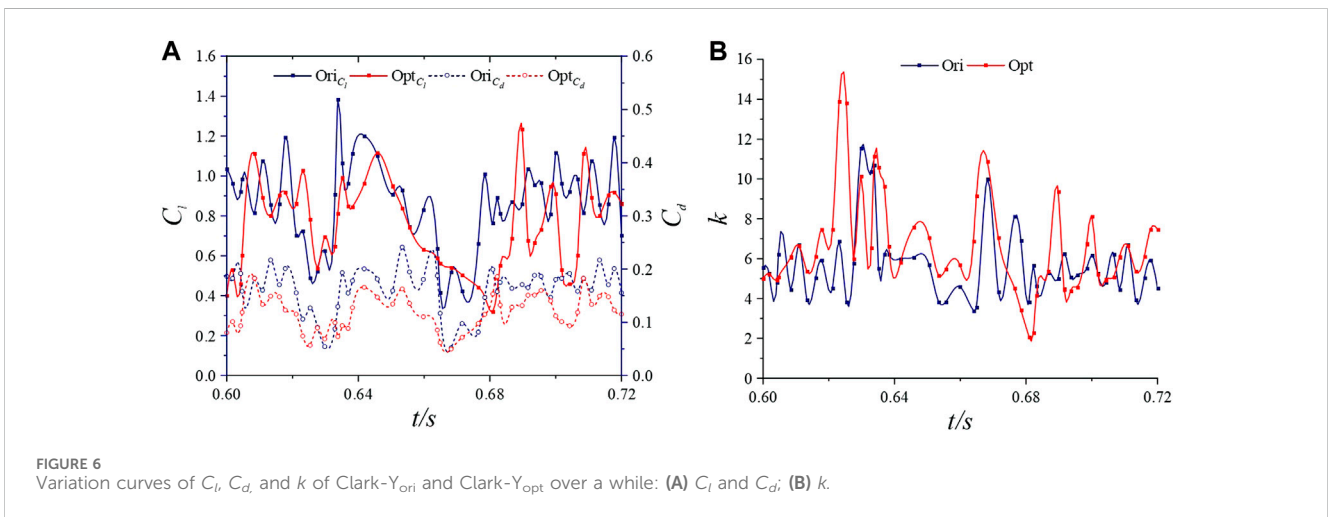
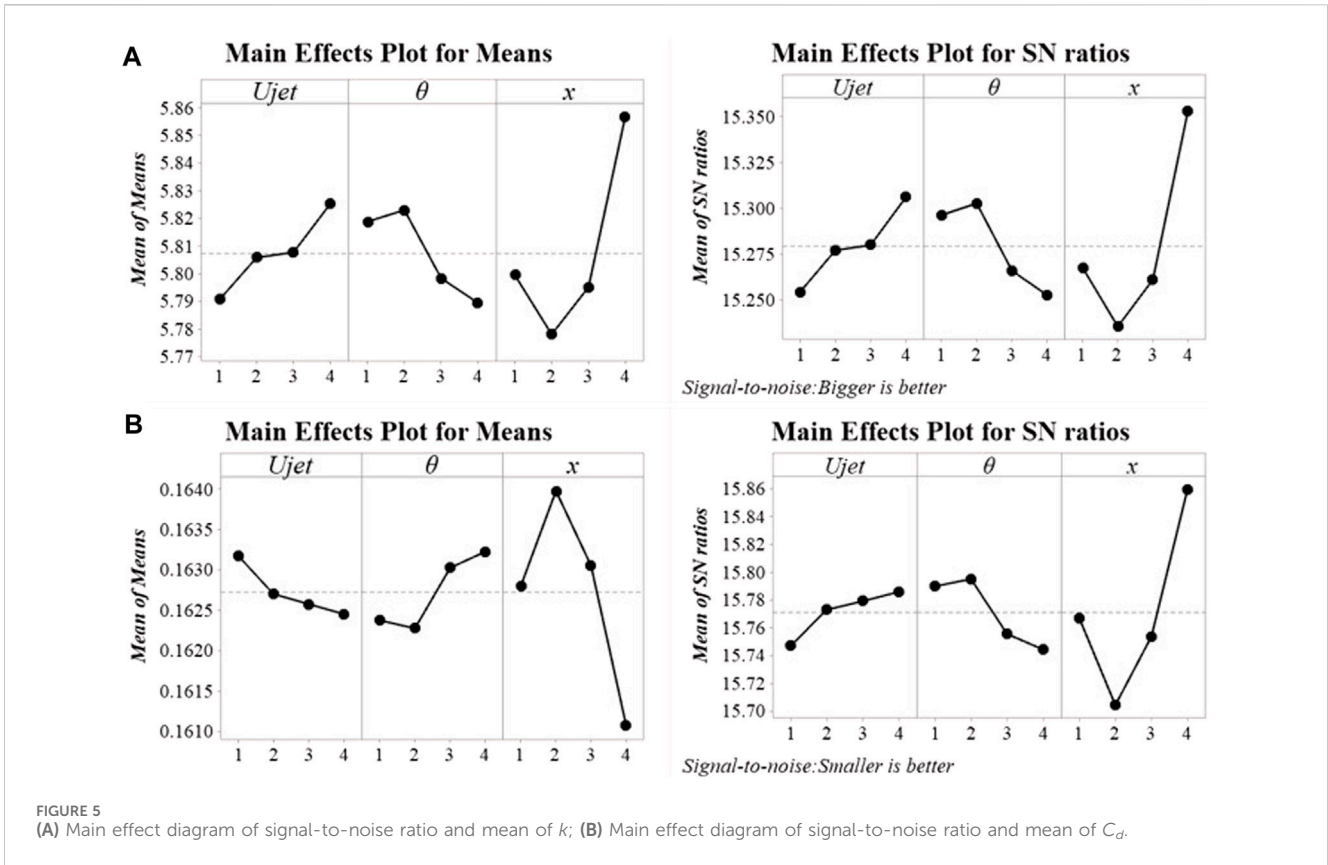


TABLE 8 Comparison of C_l , C_d and k averages of Clark- Y_{ori} and Clark- Y_{opt} schemes in the same period.

	C_l	C_d	k
Clark- Y_{ori}	0.882	0.162	5.717
Clark- Y_{opt}	0.744	0.119	6.659
Rate of change	-12.2%	-26.5%	16.4%

Clark- Y_{opt} increases relatively at $1/8t$ and gradually increases after the jet structure, indicating that the jet structure does not play a good drag reduction effect at $1/8t$. From $2/8t$ to $3/8t$, the wall shear stress of Clark- Y_{opt} decreases significantly, and the decrease is most remarkable near the jet structure. This finding is caused by the jet that blocks the return flow near the wall of the hydrofoil, resulting in a relatively average velocity distribution near the wall of the hydrofoil. Consequently, the friction resistance is reduced. At $4/8t$,

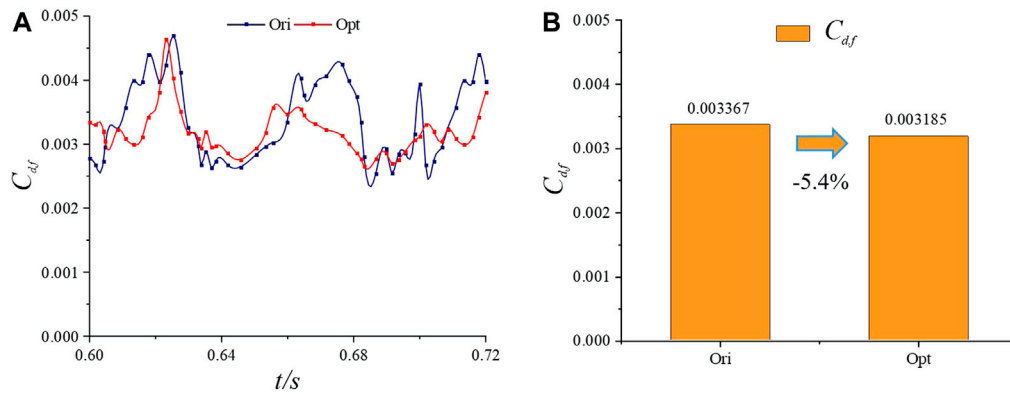


FIGURE 7 Friction resistance coefficient $C_{d,f}$ of Clark- Y_{ori} and Clark- Y_{opt} over a while: (A) transient change curve; (B) averaging results and drag reduction over the same period.

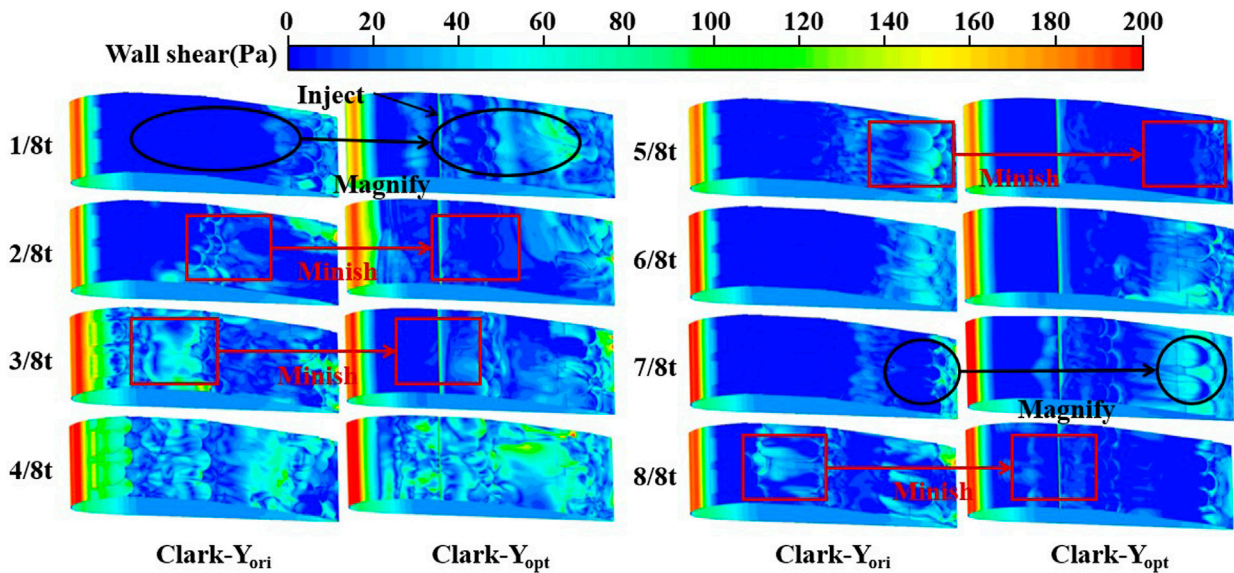


FIGURE 8 Transient shear stress distribution of Clark- Y_{ori} and Clark- Y_{opt} over a while 4.3 Pressure differential resistance and pressure analysis.

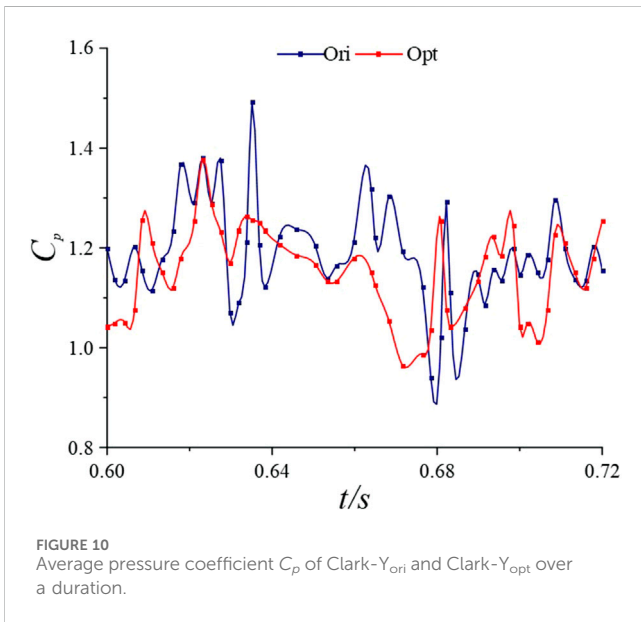
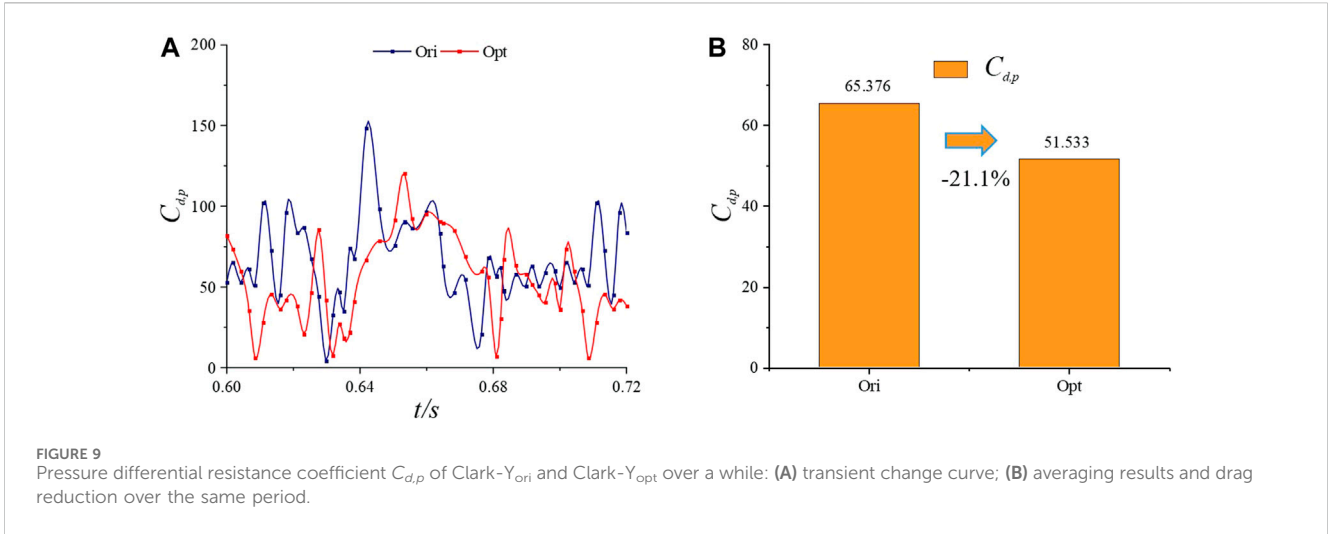
the wall shear stress of Clark- Y_{opt} has no significant change. The shear stress at the trailing edge of Clark- Y_{opt} decreased significantly at 5/8 t. However, it did not change remarkably at 6/8 t, and increased at 7/8 t. At 8/8 t, the wall shear stress of Clark- Y_{opt} decreases evidently, and this effect is mostly concentrated near the jet structure. It also decreases at the tail edge of the hydrofoil.

In general, after the addition of a jet structure, the friction resistance of the hydrofoil is reduced to a certain extent, because the jet minimises the shear stress near the wall of the hydrofoil. However, the reduction of friction resistance does not play a good role in the early stage, and this drag reduction effect becomes increasingly important with the increase in time.

As shown in Figure 9, in terms of the transient change in pressure differential resistance coefficient, Clark- Y_{opt} is significantly lower than Clark- Y_{ori} in most of the same period.

However, it increases slightly in part of the time, which is reflected in the average result. The reduction in the pressure differential resistance coefficient reached 21.1%.

As shown in Figures 10, 11, to further analyse the effect of fish scale structure on the reduction of pressure differential resistance, we examined the pressure coefficient and its transient changes under the two schemes, in which the pressure coefficient was defined as $C_p = 2p/\rho U_{\infty}^2$. As shown in Figure 10, results of analysis and comparison suggest that the fluctuation range of the pressure coefficient of Clark- Y_{opt} is smaller than that of Clark- Y_{ori} . Such stable pressure change is important for the reduction of pressure differential resistance, indicating that the jet can balance the change in the low-pressure region to a certain extent. Figure 11 shows the high-pressure areas in front of the hydrofoil and low-pressure areas on the suction side. The distribution and size of the low-pressure



area change with the flow of hydrofoil around, significantly affecting the pressure differential resistance. Specific analysis is as follows: compared with Clark- Y_{ori} , the low-pressure area at the trailing edge of Clark- Y_{opt} increases from $1/8 t$ to $2/8 t$, thereby increasing the pressure differential resistance of Clark- Y_{opt} . At $3/8 t$, the area of the low-pressure region on the suction side of Clark- Y_{opt} decreases significantly because the jet structure reduces the area of the low-pressure region by supplementing the fluid to the low-pressure region. This effect continues until $5/8 t$. At $6/8 t$, the area of the low-pressure region of Clark- Y_{opt} increases slightly, indicating that the drag reduction effect of the jet structure is weakened when the area of the low-pressure region is large. Until $7/8 t$, the effect of jet structure on the area of the low-pressure region becomes evident. At $8/8 t$, the low-pressure region on the suction side of Clark- Y_{opt} is greatly reduced, effectively decreasing the pressure differential resistance.

In general, the jet structure remarkably affects the reduction of pressure differential resistance. The jet can effectively reduce the area of the low-pressure region, minimising the pressure differential resistance of the hydrofoil. However, when the area of the low-pressure region is large, the drag reduction effect of the jet structure is weakened to a certain extent.

4.3 Analysis of turbulence intensity

In addition to effectively minimising friction resistance and pressure differential resistance, the flow state of the fluid is important for drag reduction. It can effectively suppress turbulence, promoting a transition towards laminar flow state and further reducing resistance. On this basis, we further analyse the turbulence strength of the fluid, defined as follows: $I = ((V_x^2 + V_y^2 + V_z^2)/3)^{1/2}/V_{avg}$, where V_x , V_y and V_z represent the x , y and z directions of speed pulsating quantity, respectively, and V_{avg} is the average speed. As shown in Figure 12, the turbulence intensity of Clark- Y_{opt} is smaller than that of Clark- Y_{ori} most of the time, reflecting the average result. The reduction rate of turbulence intensity is 4.9%.

To further compare the turbulence intensity of the two schemes, the transient turbulence intensity distribution was analysed, as shown in Figure 13. Compared with Clark- Y_{ori} , the turbulence intensity distribution on the suction side of Clark- Y_{opt} did not change significantly from $1/8 t$ to $2/8 t$. The turbulence intensity on the suction side of Clark- Y_{opt} did not decrease until $3/8 t$, and the turbulence intensity near the jet structure decreased significantly. This inhibition effect on turbulence continued until $6/8 t$, and at $5/8 t$ and $6/8 t$, the turbulence intensity on the suction side of Clark- Y_{opt} decreased significantly. This finding shows that the jet can effectively inhibit the further development of turbulence during the turbulent flow. At $7/8 t$, the turbulence intensity at the trailing edge of Clark- Y_{opt} increases slightly and does not decrease significantly until $8/8 t$.

In general, the jet structure does not play an excellent role in inhibiting turbulence when it appears, but can effectively inhibit its

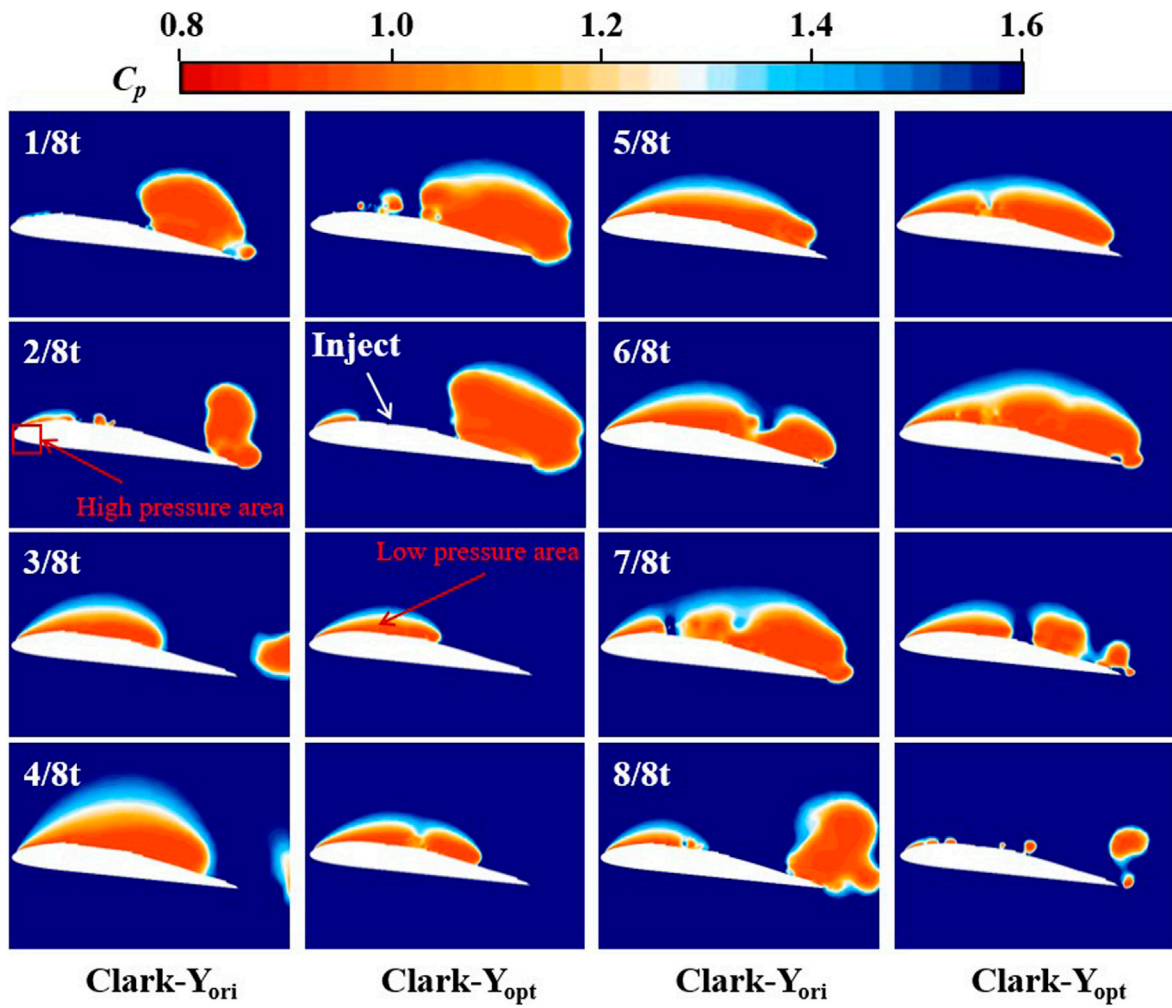


FIGURE 11 Distribution of transient pressure coefficients of Clark- Y_{ori} and Clark- Y_{opt} over a duration.

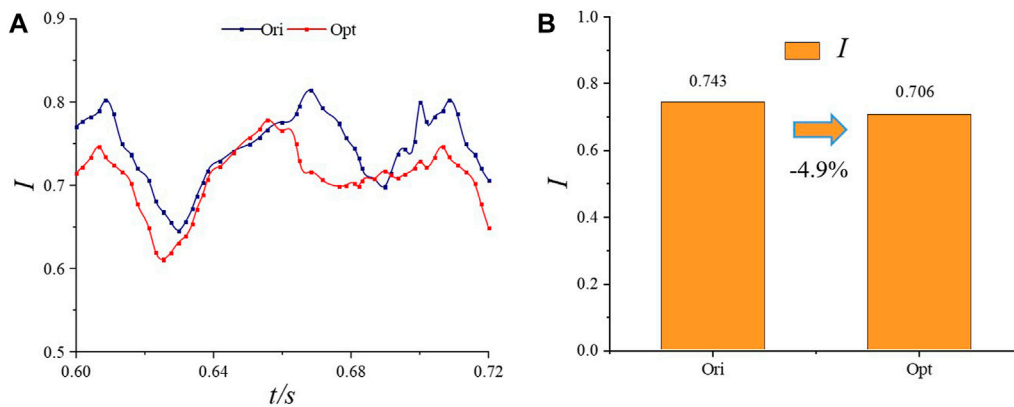


FIGURE 12 Turbulence intensity of Clark- Y_{ori} and Clark- Y_{opt} over a duration I : (A) transient curve; (B) averaging results and reduction rates over the same period.

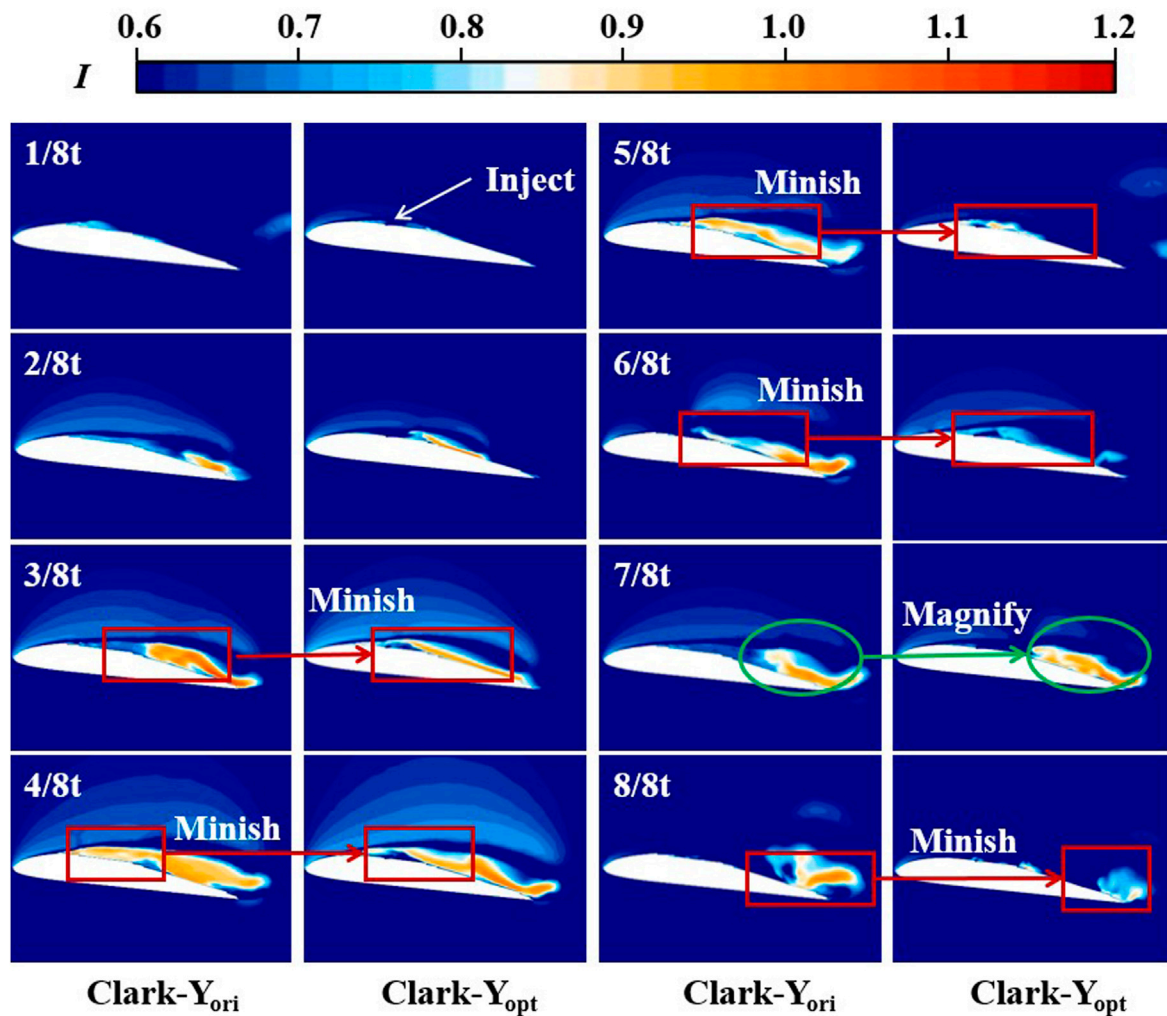


FIGURE 13 Transient turbulence intensity of Clark- Y_{ori} and Clark- Y_{opt} over a duration t .

further development. This approach is important for effectively reducing turbulence resistance.

4.4 Vorticity analysis

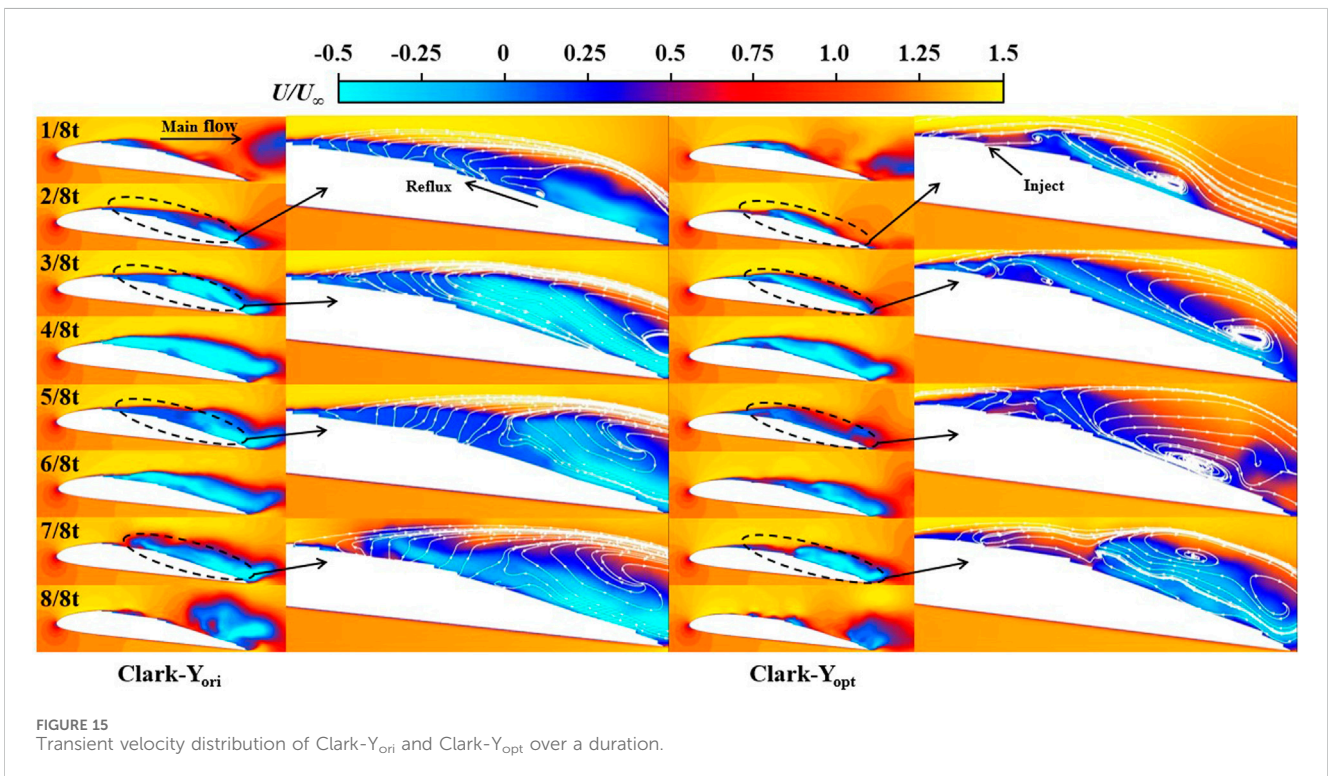
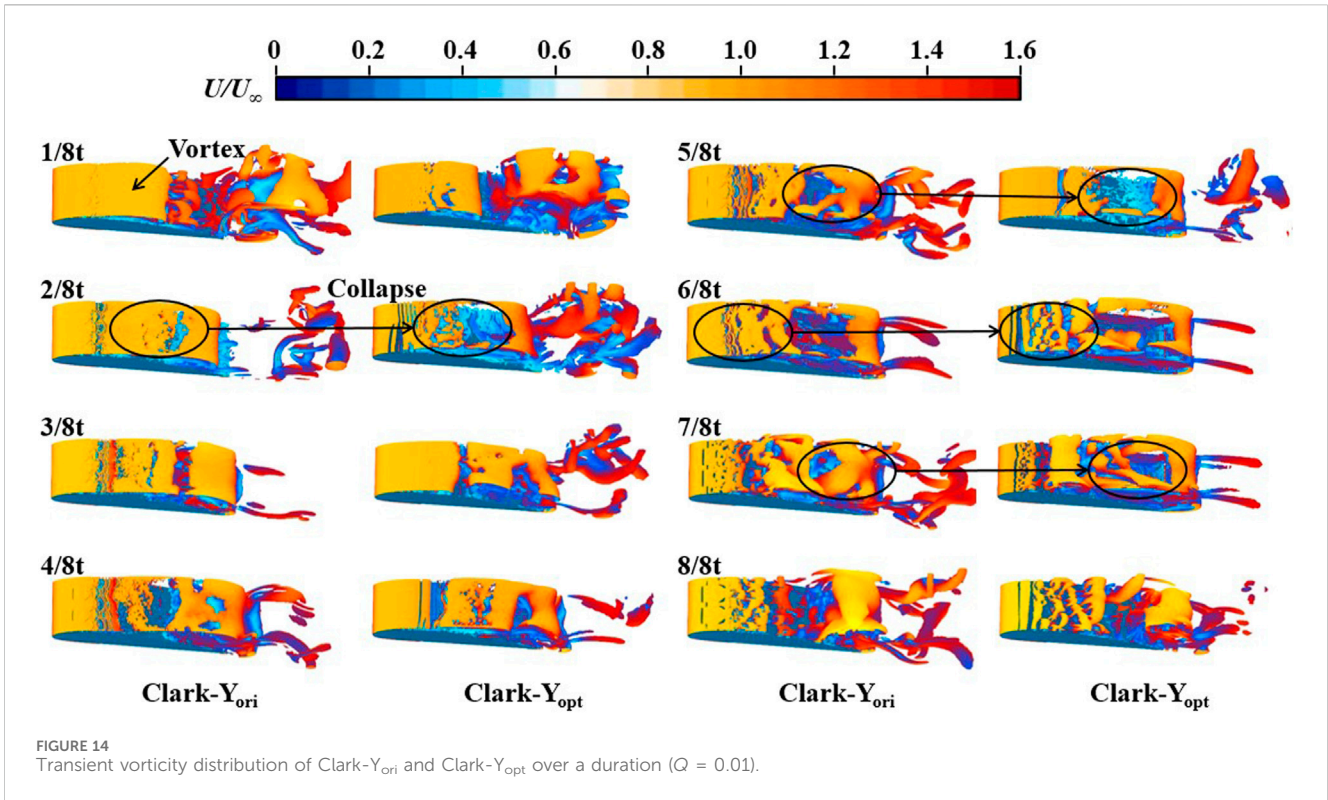
As shown in Figure 14, to further analyse how fish scale structure reduces turbulence intensity, the generation, development and shedding of vortices were further discussed under the Q criterion. The specific analysis is as follows: at $1/8 t$, vortices appear near the leading edge of the hydrofoil. Compared with Clark- Y_{ori} , the vortices on the suction side of Clark- Y_{opt} begin to collapse due to the jet structure. At $2/8 t$, the vortices on the suction side of Clark- Y_{opt} begin to collapse in a large area, indicating that the jet accelerates the collapse of vortices to suppress turbulence. From $3/8 t$ to $4/8 t$, no significant change was observed between the two schemes, until $5/8 t$ when the vortex at the trailing edge of Clark- Y_{opt} began to collapse in a large area. At $6/8 t$, the vortex began to fall off towards the trailing edge, and the vortex near the jet structure of Clark- Y_{opt} further collapsed. This accelerated collapse effect on the

vortex lasted until $7/8 t$. At $8/8 t$, the vortices of the two schemes have fallen off near the trailing edge, but the vortices of Clark- Y_{opt} are relatively small.

In general, the jet structure accelerates the collapse of the vortex. This effect is evident in the vortex generation, and a more significant effect is observed on the development and shedding of the subsequent vortex. Consequently, the turbulence is inhibited and transformed into a laminar flow state to further reduce the turbulence resistance.

4.5 Speed analysis

Previously, we analysed that the fish scale structure can effectively reduce friction resistance, pressure differential resistance and turbulence resistance. To further observe the drag reduction effect, we further examined the velocity distribution around the hydrofoil. As shown in Figure 15, because Clark- Y_{opt} has a jet drag-reducing structure, the velocity around its hydrofoil is relatively higher. It is reflected in the cloud image, namely, a larger



high-speed mainstream area and a smaller low-speed reflux area. Moreover, a smaller low-speed reflux area indicates that the internal friction between the mainstream and reflux can be more effectively reduced. Specific analysis is as follows: compared with Clark- Y_{ori} , no

significant difference in velocity distribution is observed between the two schemes at $1/8 t$ because no evident reflux exists on the hydrofoil near the wall at this time. Thus, the effect of jet structure on blocking reflux is weak. At $2/8 t$, the near-wall reflux of hydrofoil begins to

appear, at which time the jet structure of Clark- Y_{opt} plays a role in blocking the reflux; it still has a certain blocking effect until $3/8 t$. Therefore, the low-speed reflux area of Clark- Y_{opt} is smaller than that of Clark- Y_{ori} . In addition, at $4/8 t$, the reflux area reaches the maximum. When the reflux velocity is higher, the blocking effect of the jet structure becomes weakened. At $5/8 t$, the low-speed return area of both schemes decreases relatively. However, the low-speed return area of Clark- Y_{opt} is smaller. Until $8/8 t$, the jet structure can effectively inhibit the internal friction between fluids and efficiently reduce the resistance.

In general, the jet structure can inhibit the return flow near the wall and effectively reduce the internal friction resistance of the fluid. Therefore, the speed of the suction side of Clark- Y_{opt} is relatively higher, confirming the reduction of various resistances analysed in the previous section.

5 Conclusion

On the basis of the intermittent fish scale drag reduction structure, a bionic jet drag reduction idea, which organically combined the fish scale drag reduction and jet drag reduction, is proposed. The results show the optimal parameter combination through the Taguchi algorithm, as follows: $U_{jet} = 1.44 \text{ m/s}$, $\theta = 3^\circ$ and $x = 18.6 \text{ mm}$. The drag reduction effect of the two schemes was further analysed through large eddy simulation. The lift resistance characteristics, friction resistance and shear stress, pressure difference resistance and pressure distribution, turbulence intensity, vorticity distribution and velocity distribution were assessed, and the following conclusions were obtained:

- (1) Compared with Clark- Y_{ori} , the lift force of Clark- Y_{opt} is reduced, but it still has better drag reduction effect. Whilst reducing drag, the lift-drag ratio of hydrofoil is greatly increased and the hydraulic performance of hydrofoil is improved.
- (2) The friction resistance analysis indicates that a jet can effectively reduce the shear stress of the hydrofoil wall, thereby diminishing the friction resistance. The analysis of pressure differential resistance also indicated that the pressure fluctuation on the suction side of Clark- Y_{opt} with jet structure is relatively stable, which is important for the reduction in pressure differential resistance. Moreover, Clark- Y_{opt} can effectively decrease the pressure difference between the leading edge and the tail edge of the hydrofoil, greatly minimising the pressure differential resistance. This drag reduction effect is relatively weakened.
- (3) For the fluid flow state near the hydrofoil, the jet structure can effectively inhibit the occurrence of turbulence and transform the fluid into laminar flow state, reducing the turbulence resistance. Further analysis of the vorticity distribution on the suction side of the hydrofoil suggested that the jet structure accelerates the collapse of the vorticity to achieve turbulence suppression.

- (4) The analysis of the velocity distribution around the hydrofoil indicated that the mainstream velocity of Clark- Y_{opt} is higher and the area of the high-speed region is relatively larger. This condition is caused by the jet structure that blocks the reflux and greatly weakens the internal friction between the mainstream and the reflux, verifying the drag-reduction effect of the jet structure to a certain extent.

Author contributions

HY: Conceptualization, Formal Analysis, Methodology, Writing–review and editing. TX: Data curation, Funding acquisition, Software, Validation, Writing–original draft, Writing–review and editing. JL: Formal Analysis, Funding acquisition, Software, Supervision, Writing–review and editing. JF: Data curation, Funding acquisition, Investigation, Validation, Writing–original draft. XD: Data curation, Funding acquisition, Project administration, Software, Writing–original draft.

Funding

The author(s) declare that financial support was received for the research, authorship, and/or publication of this article. This work was supported by the Fundamental Research Funds for the Central Universities (NO: JZ2021HGTB0090), the University Synergy Innovation Program of Anhui Province under Grant No. GXXT-2019-004, the financial support provided by the National Natural Science Foundation of China (51806053).

Acknowledgments

The authors are grateful for the support of the National Natural Science Foundation of China.

Conflict of interest

The authors declare that the research was conducted in the absence of any commercial or financial relationships that could be construed as a potential conflict of interest.

Publisher's note

All claims expressed in this article are solely those of the authors and do not necessarily represent those of their affiliated organizations, or those of the publisher, the editors and the reviewers. Any product that may be evaluated in this article, or claim that may be made by its manufacturer, is not guaranteed or endorsed by the publisher.

References

- Bai, L., Yang, Y., Zhou, L., Li, Y., Xiao, Yu, and Shi, W. (2022). Optimal design and performance improvement of an electric submersible pump impeller based on Taguchi approach. *Energy* 252 (2022), 124032. doi:10.1016/j.energy.2022.124032
- Chen, K., Wei, Z. G., Lin, Y. S., Zhao, X. F., Qi, X., Huang, C. H., et al. (2021). IOP conf. Series: earth and environmental science. *IOP Conf. Ser. Earth Environ. Sci.* 701, 012056. doi:10.1088/1755-1315/701/1/012056
- Dou, Z., Wang, J., and Chen, D. (2012). Bionic research on fish scales for drag reduction. *J. Bionic Eng.* 9, 457–464. doi:10.1016/s1672-6529(11)60140-6
- Feng, G., Lei, S., Guo, Y., Shi, D., and Shen, J. B. (2020b). Optimisation of air-distributor channel structural parameters based on Taguchi orthogonal design. *Case Stud. Therm. Eng.* 21, 100685. doi:10.1016/j.csite.2020.100685
- Feng, Y.-Y., Hu, H., Peng, G.-Yi, and Zhou, Yu (2020a). Microbubble effect on friction drag reduction in a turbulent boundary layer. *Ocean. Eng.* 211, 107583. doi:10.1016/j.oceaneng.2020.107583
- Ganesh Natarajan, S., and Bruce Ralphin Rose, J. (2022). Performance enhancement of futuristic airplanes by nature inspired biomimetic fish scale arrays—a design approach. *Biomim. Intell. Robotics* 2 (2022), 100045. doi:10.1016/j.birob.2022.100045
- Gu, Y., Zhao, G., Zheng, J., Li, Z., Liu, W., and Muhammad, F. K. (2014). Experimental and numerical investigation on drag reduction of non-smooth bionic jet surface. *Ocean. Eng.* 81, 50–57. doi:10.1016/j.oceaneng.2014.02.015
- Kim, Y., Roh, T.-S., Huh, H., and Lee, H. J. (2020). Study on the combined effect of various injection conditions on the drag reduction by a counter-flow jet in supersonic flow. *Aerosp. Sci. Technol.* 98, 105580. doi:10.1016/j.ast.2019.105580
- Kotcioglu, I., Cansiz, A., and Nasiri Khalaji, M. (2013). Experimental investigation for optimization of design parameters in a rectangular duct with plate-fins heat exchanger by Taguchi method. *Appl. Therm. Eng.* 50, 604–613. doi:10.1016/j.applthermaleng.2012.05.036
- Li, F., Zhao, G., and Liu, W. (2017). Research on drag reduction performance of turbulent boundary layer on bionic jet surface. *Proc IMechE Part M J Eng. Marit. Environ.* 231 (1), 258–270. doi:10.1177/1475090216642463
- Liu, B., Xu, X., Pan, D., and Wang, X. (2023). Research on shipping energy-saving technology: hydrofoil amphibious vehicle driven by waterjet propulsion. *J. Clean. Prod.* 382 (2023), 135257. doi:10.1016/j.jclepro.2022.135257
- Lv, K., Liu, Y., You, C., Zou, Y., Shi, Z., Lv, P., et al. (2013). Hydrodynamic investigations of a cross-domain vehicle with the capability of high-speed cruising on water surface. *Ocean Engineering* 25 (6), 944–953.
- Muthuramalingam, M., Puckert, D. K., Rist, U., and Bruecker, C. (2020). Transition delay using biomimetic fish scale arrays. *Sci. Rep.* 10 (1), 14534. doi:10.1038/s41598-020-71434-8
- Muthuramalingam, M., Villemin, L. S., and Bruecker, C. (2019). Streak formation in flow over biomimetic fish scale arrays. *J. Exp. Biol.* 222 (16), jeb205963. doi:10.1242/jeb.205963
- Nowrouz Mohammad, N., Mohammad Saadat, B., and Setareh, S. (2013). Analysis of shear rate effects on drag reduction in turbulent channel flow with superhydrophobic wall. *J. Hydrodynamics* 25 (6), 944–953. doi:10.1016/s1001-6058(13)60444-8
- Nowrouz Mohammad, N., Setareh, S., and Alireza, M. (2012). Drag reduction in a turbulent channel flow with hydrophobic wall. *J. Hydrodynamics* 24 (3), 458–466. doi:10.1016/s1001-6058(11)60267-9
- Park, H. J., Tasaka, Y., Oishi, Y., and Murai, Y. (2015). Drag reduction promoted by repetitive bubble injection in turbulent Channelflows. *Int. J. Multiph. Flow* 75, 12–25. doi:10.1016/j.ijmultiphaseflow.2015.05.003
- Shen, B. X., Liu, W. Q., and Yin, L. (2018). Drag and heat reduction efficiency research on opposing jet in supersonicflows. *Aerosp. Sci. Technol.* 77, 696–703. doi:10.1016/j.ast.2018.03.051
- Shen, H., Xiao, Q., Zhou, J., Su, Y., and Bi, X. (2022). Design of hydrofoil for the resistance improvement of planing boat based on CFD technology. *Ocean. Eng.* 255 (2022), 111413. doi:10.1016/j.oceaneng.2022.111413
- Wang, F., Yan, H., Zeng, Y. S., Xu, W., Zang, H. Z., and Meng, J. (2021a). Design optimization of a fluidized bed with a novel air chamber using the CFD-Taguchi method. *Proc. IMechE Part C. J. Mech. Eng. Sci.* (0), 1–14. doi:10.1177/09544062211029325
- Wang, F., Yan, H., Zeng, Y. S., Xu, W., Zang, H. Z., and Meng, J. (2021b). Design of a novel flat-cloth airway in powder tank based on Taguchi optimization. *Proc. IMechE Part C. J. Mech. Eng. Sci.* (0), 1–13. doi:10.1177/09544062211010864
- Wang, G., Senocak, I., Shyy, W., Ikohagi, T., and Cao, S. (2001). Dynamics of attached turbulent cavitating flows. *Prog. Aero. Sci.* 37, 551–581. doi:10.1016/s0376-0421(01)00014-8
- Wang, Y., Zhang, Z., Xu, J., and Yu, H. (2021). One-step method using laser for large-scale preparation of bionic superhydrophobic & drag-reducing fish-scale surface. *Surf. Coatings Technol.* 409 (2021), 126801. doi:10.1016/j.surfcoat.2020.126801
- Yagiz, B., Kandil, O., and Volkan Pehlivanoglu, Y. (2012). Drag minimization using active and passiveflow control techniques. *Aerosp. Sci. Technol.* 17, 21–31. doi:10.1016/j.ast.2011.03.003
- Yan, H., Jian, Li a, Wu, M., Xie, C., Liu, C., and Qi, F. (2022). Study on the influence of active jet parameters on the cavitation performance of Clark-Y hydrofoil. *Ocean. Eng.* 261 (2022), 111900. doi:10.1016/j.oceaneng.2022.111900
- Yan, H., Su, X. Z., Zhang, H. Z., Hang, J. W., Zhou, L., Liu, Z. F., et al. (2020). Design approach and hydrodynamic characteristics of a novel bionic airfoil. *Ocean. Eng.* 216, 108076. doi:10.1016/j.oceaneng.2020.108076
- Yan, H., Zhang, H. Z., Zeng, Y. S., and He, X. Y. (2021). Lift-drag characteristics and unsteady cavitating flow of bionic hydrofoil. *Ocean. Eng.* 225, 108821. doi:10.1016/j.oceaneng.2021.108821
- Zhang, J., Gabillet, C., and Billard, J.-Y. (2021). Experimental study of the bubbly drag reduction in the recovery region of a separated turbulent boundary layer. *Int. J. Multiph. Flow* 142 (2021), 103697. doi:10.1016/j.ijmultiphaseflow.2021.103697